






# Protons in (Ga,Sc,In,Y)<sup>3+</sup>-doped BaFeO<sub>3</sub> triple conductors — Site energies and migration barriers investigated by density functional theory calculations

A. Chesnokov<sup>a,b</sup> , D. Gryaznov<sup>a</sup> , E.A. Kotomin<sup>a,c</sup> , J. Maier<sup>c</sup> , R. Merkle<sup>c,\*</sup> 

<sup>a</sup> Institute of Solid State Physics, University of Latvia, Riga, Latvia

<sup>b</sup> present address: School of Optoelectronic Engineering & CQUPT-BUL Innovation Institute, Chongqing University of Posts and Telecommunications, Chongqing, China

<sup>c</sup> Max Planck Institute for Solid State Research, Stuttgart, Germany

## ARTICLE INFO

### Keywords:

Triple conducting perovskites  
Proton trapping  
Proton transfer barriers  
Density functional theory  
Protonic ceramic fuel and electrolysis cells

## ABSTRACT

BaFeO<sub>3-δ</sub> is a prototypical “triple-conducting” perovskite combining electronic, proton and oxygen vacancy conductivities. Here, the interaction energies of protons at different sites with Ga<sup>3+</sup>, Sc<sup>3+</sup>, In<sup>3+</sup>, and Y<sup>3+</sup> dopants on the Fe site in BaFeO<sub>3</sub> are calculated using density functional theory (DFT). The effect of the dopants on the respective proton transfer barriers is also investigated. While for the smaller Ga<sup>3+</sup> and Sc<sup>3+</sup> dopants a slight trapping of protons in the first and second shell around the dopant is found, in the case of the strongly oversized In<sup>3+</sup> and Y<sup>3+</sup> the first shell exhibits a repulsive behaviour for protons (despite attractive electrostatic interaction). The calculated proton transfer barriers for different configurations depend sensitively on the local geometry. They follow the previously derived correlations with O-H bond lengths and O···O distances in BaFeO<sub>3-δ</sub>, corroborating that these quantities are physically meaningful descriptors for proton transfer in perovskites. Overall, a very complex energy landscape is obtained, and the consequences for long-range proton transport are discussed only qualitatively. The combination of a proton-repulsive first shell and the tendency for increased proton barriers suggests that for BaFeO<sub>3-δ</sub>, instead of the very oversized Y<sup>3+</sup> smaller dopants should be considered.

## 1. Introduction

Materials that combine good electronic transport with perceptible proton conductivity (and typically also mobile oxygen vacancies) are key functional materials in protonic ceramic fuel and electrolysis cells (PCFC, PCEC), as demonstrated e.g. in [1–7]. Typically, these materials have perovskite structure (or closely related structures such as double perovskites [3,8] or Ruddlesden-Popper phases [9,10]) and exhibit mobile oxygen vacancies. The perovskite ABO<sub>3</sub> structure offers several important advantages: (i) High compositional flexibility, i.e. point defect concentrations and other properties can be tuned by doping on the A- and B-site. (ii) B-O-B connections which are linear (or only slightly distorted from 180°). This allows for good overlap of O-2p and B-3d orbitals resulting in high mobility of electronic carriers. (iii) Typically high symmetry (cubic structure, or only slight distortions from it) which is favourable for the mobility of the ionic carriers such as oxygen vacancies (V<sub>O</sub><sup>••</sup> [11,12]) and protonic defects (OH<sub>O</sub><sup>•</sup> [13]), because several

equivalent sites are available for the transfer of these carriers.

Experimentally, it is found that the degree of hydration is lower in (Ba,Sr,Ln)(Fe,Co,M)O<sub>3-δ</sub> triple conductors compared to electrolyte-type Ba(Ce,Zr,Dop)O<sub>3-δ</sub> perovskites [2,4,14]. Often, oversized dopants (lower-valent Dop<sup>3+</sup> or Dop<sup>2+</sup>, but even isovalent dopants such as Zr<sup>4+</sup>, Ce<sup>4+</sup>, Sn<sup>4+</sup>) are found to be beneficial for the proton uptake (e.g. [14,15]) although undoped BaFeO<sub>3-δ</sub> already exhibits a perceptible V<sub>O</sub><sup>••</sup> concentration. To achieve the required proton conductivity, also the proton mobility needs to be considered. Owing to the challenge to separate the proton conductivity from V<sub>O</sub><sup>••</sup> conductivity and the orders of magnitude higher electronic conductivity, experimental data on proton mobilities of triple conductors are rare. Using DFT calculations, relatively low proton transfer barriers of 0.18–0.22 eV were found for undoped BaFeO<sub>3-δ</sub> [16], which is even lower than for BaZrO<sub>3</sub> treated with the same methodology. The effect of dopants on proton mobility in triple conductors, including long-range transport, has not been investigated in detail yet.

\* Corresponding author.

E-mail address: [r.merkle@fkf.mpg.de](mailto:r.merkle@fkf.mpg.de) (R. Merkle).

<https://doi.org/10.1016/j.ssi.2025.116788>

Received 22 November 2024; Received in revised form 16 January 2025; Accepted 17 January 2025

Available online 1 February 2025

0167-2738/© 2025 The Authors. Published by Elsevier B.V. This is an open access article under the CC BY-NC-ND license (<http://creativecommons.org/licenses/by-nc-nd/4.0/>).

For the archetypical electrolyte material BaZrO<sub>3</sub>, Y<sup>3+</sup> has been identified as the dopant with the most suitable size for achieving a high bulk proton conductivity [13]. However, this choice can not simplistically be applied for BaFeO<sub>3-δ</sub> triple conductors, which have a significantly smaller lattice parameter relative to BaZrO<sub>3</sub> (4.04 Å vs. 4.20 Å) and also a higher covalency of Fe-O compared to Zr-O bonds. For BaZrO<sub>3</sub>, defect interactions between dopants and protons have been observed experimentally: variation of effective proton mobility with dopant element (e.g. [13]) and concentration (e.g. [17,18]), comparison of short- and long-range transport [19], and NMR experiments [20,21]. Also quantum-chemical investigations (e.g. [20–24]) indicate perceptible defect interactions comprising proton trapping in first and second shell around the dopant, and modified proton transfer barriers. Owing to the combined effect of defect interactions the proton conductivity can not be described by a simplistic “2-state trapping model” [25].

Here we explore the effect of different B-site dopants on proton trapping and migration barriers in triple-conducting BaFeO<sub>3</sub> using DFT calculations. This also allows us to analyse initial and transition state geometries in detail. Ab-initio calculations are required, because proton transfer means breaking of covalent O-H bonds, and also because the Fe-O bonds have a high and variable degree of covalency (depending on local distortions [26,27]). So far, only a few publications report calculated proton transfer barriers in triple conductors (e.g. [28–31]), but a systematic study including various dopants is not available yet. Results of the present static DFT calculations including barriers from the nudged elastic band approach (NEB) indicate that in presence of dopants protons in BaFeO<sub>3</sub> experience a really complex energy landscape, in which site energies as well as migration barriers depend on multiple parameters and long-range transport depends sensitively on type, concentration, and configuration of the dopants. While we are aware of the limitations of static DFT calculations for such systems, the present calculations already yield important information about dopant optimization in BaFeO<sub>3-δ</sub>. A next step would be molecular dynamics simulations. For a material with correlated electrons this would be computationally much more demanding on ab initio level than for a large-bandgap system such as BaZrO<sub>3</sub>. The emerging approach of machine learning potentials derived from DFT data (e.g. [32–36]) might in the future help to bridge this gap.

The present investigation considers Ga<sup>3+</sup>, Sc<sup>3+</sup>, In<sup>3+</sup>, and Y<sup>3+</sup> dopants which cover a range of size and bonding character [37,38], as used already for BaZrO<sub>3</sub> [22] and BaCeO<sub>3</sub>-BaFeO<sub>3</sub> composites [39]. We concentrate on site energies and barriers for protons (the calculation of hydration energies according to H<sub>2</sub>O + V<sub>O</sub><sup>••</sup> + O<sub>O</sub><sup>x</sup> = 2 OH<sub>O</sub><sup>•</sup> would require an extended investigation of dopant-V<sub>O</sub><sup>••</sup> interactions).

## 2. Computational details

The VASP 6.1 code, the projector augmented wave method and scalar relativistic pseudopotentials (i.e., PAW potential as according to VASP calculations nomenclature) were used [40–43]. The PAW potentials were chosen with 10 valence electrons on Ba, 14 on Fe (Fe 3p<sup>6</sup> electrons also treated as valence electrons), 6 on O, and 1 on H (Table 1). These are the same PAW potentials as in our previous work on undoped BaFeO<sub>3</sub> [16,44]. The dopant atoms were also treated with the inclusion of electrons from semi-core s- and p-orbitals for Y and Sc and closed d-

**Table 1**  
PAW potential data used in the present study.

Atom	Valence electrons	Cut-off energy / eV
Ba	5s <sup>2</sup> 5p <sup>6</sup> 5d <sup>0.01</sup> 6s <sup>1.99</sup>	187.181
Fe	3p <sup>6</sup> 3d <sup>7</sup> 4s <sup>1</sup>	293.238
O	2s <sup>2</sup> 2p <sup>4</sup>	400.000
H	1s <sup>1</sup>	250.000
Y	4s <sup>2</sup> 4p <sup>6</sup> 4d <sup>2</sup> 5s <sup>1</sup>	202.626
Sc	3s <sup>2</sup> 3p <sup>6</sup> 3d <sup>2</sup> 4s <sup>1</sup>	222.660
Ga	3d <sup>10</sup> 4s <sup>2</sup> 4p <sup>1</sup>	282.691
In	4d <sup>10</sup> 5s <sup>2</sup> 5p <sup>1</sup>	239.211

orbitals for Ga and In. The chosen PAW potentials increase the computational cost due to a larger number of valence electrons and increased cut-off energy but also increase the accuracy of the obtained results in the comparison with more standard PAW potentials. The exchange-correlation GGA-type functional is that of Perdew, Burke, and Ernzerhof (PBE) [45].

We employ rotationally invariant Dudarev-form PBE +  $U_{\text{eff}}$  calculations [46], using an effective  $U_{\text{eff}} = U - J$  (hereafter, simply  $U$ ) parameter to treat the strong correlation effects for Fe 3d electrons. A fixed  $U = 4.0$  eV is chosen for Fe, in accordance with our previous calculations for BaFeO<sub>3</sub> [16,44], and other literature [47–49]. We choose the PBE +  $U_{\text{eff}}$  approach (instead of using hybrid functionals such as HSE06) because (i) it allows us to compare with proton barriers in undoped BaFeO<sub>3-δ</sub> [16] calculated with exactly the same methodology, (ii) test calculation in [16] indicate that HSE06 yields qualitatively very similar geometries and barriers for proton transfer, so the computationally less demanding PBE +  $U_{\text{eff}}$  suffices for the properties that are of interest here.

The plane wave energy cut-off is fixed at 500 eV, the Brillouin zone sampling of the primitive unit cell (space group Pm-3m) is taken as  $\Gamma$ -centred  $8 \times 8 \times 8$  Monkhorst-Pack mesh. The mesh was adjusted for the two supercell sizes, namely 40 atom ( $2 \times 2 \times 2$  extension of primitive cell) and 160 atom cells ( $4 \times 4 \times 2$  extension of primitive unit cell, with a single Dop<sup>3+</sup> i.e. corresponding to a decreased dopant concentration), allowing us to consider 1st, 2nd, and 3rd coordination spheres around Dop<sup>3+</sup>. The extended supercell was needed to (i) accurately calculate the full potential energy curve, i.e. system total energy as a function of Dop-H distance up to  $\sim 11$  Å (Figs. 3,4); (ii) obtain more relaxed environments for the 1st and 2nd coordination sphere. The energy criteria for the electronic and ionic structure relaxations are chosen as  $10^{-5}$  eV and  $10^{-4}$  eV, respectively. Full relaxation of internal coordinates and lattice parameters was performed without symmetry restrictions. The calculations are performed in spin-polarized mode. Fe acquires the high-spin state, which is typical for such oxides [50].

While at actual PCFC operating temperature the iron perovskites become paramagnetic, in DFT calculations we consistently keep a ferromagnetic spin alignment of the Fe ions to avoid spurious superposition of reaction energies/migration barriers with magnetic transitions, cf. [50].

Similar as for proton barriers of undoped BaFeO<sub>3</sub> [16], we investigate the doped BaFeO<sub>3</sub> materials in the perovskite structure with corner-sharing BO<sub>6</sub> octahedra (cubic or only slightly distorted from cubic). While the thermodynamically stable structure is hexagonal with face-sharing octahedra [51], it can be transformed into the metastable cubic structure by certain temperature and pO<sub>2</sub> treatment [52]. BaFeO<sub>3-δ</sub>-based materials actually applied in PCFC have the cubic perovskite structure, thermodynamically stabilized by doping with 5 % La on the Ba site [53], or B-site dopants with higher charge or larger size than iron such as Zr, Y (cf. [2,4]).

The formal Fe oxidation state in the neutral supercells applied here is always 4+ as calculated from the overall stoichiometry, so in contrast to [16] here we do not investigate effects of changing the formal Fe oxidation state on proton energies and transfer barriers (only a few data for Ba<sub>8</sub>Fe<sub>8</sub>O<sub>24</sub>H in Fig. 1 and Ba<sub>8</sub>Fe<sub>8</sub>O<sub>23</sub>H, Ba<sub>8</sub>Fe<sub>8</sub>O<sub>21</sub>H in Fig. 3 g from [16] refer to cells in which some Fe have 3+ oxidation state). However, owing to the high covalency of the Fe-O bonds the actual Fe d-orbital occupancy is close to d<sup>5</sup>L (L = ligand hole) and the effective iron oxidation state thus approaches 3+ and a ligand hole is formed [16,44]. This is similar as in other iron perovskites (e.g. [54,55]) and denotes the material as so-called negative charge transfer material.

It has to be mentioned that energy minimization in the present supercells is challenging. The cells comprise two point defects (Dop<sub>Fe</sub><sup>•</sup>, OH<sub>O</sub><sup>•</sup>), and, as discussed in more detail in [16,44], even undoped BaFeO<sub>3</sub> exhibits a Jahn-Teller type distortion pattern of the FeO<sub>6</sub> octahedra (but this lowers the energy only by 0.02 eV/f.u.). An artificial suppression of this Jahn-Teller type distortion is not feasible here because to properly

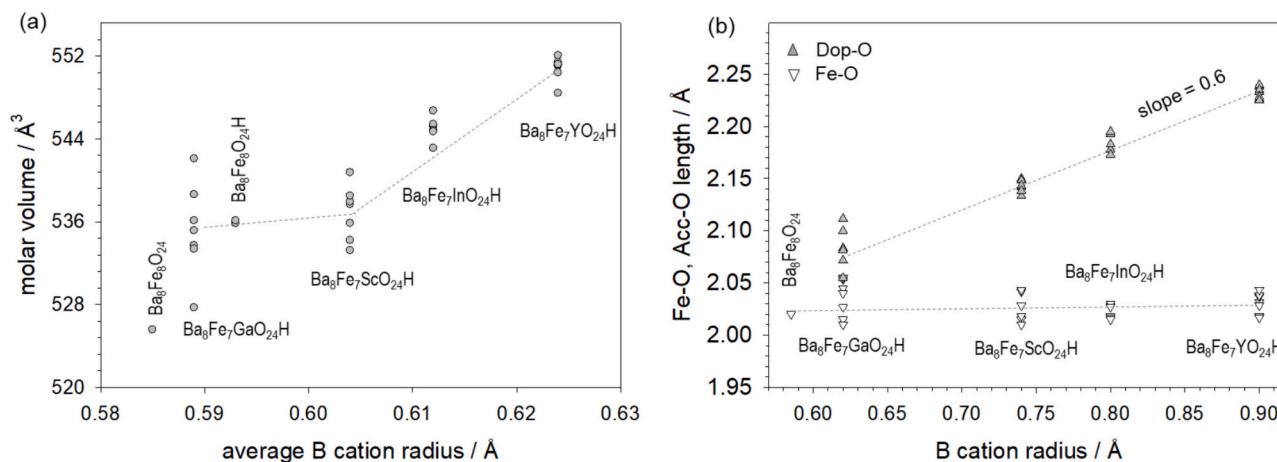


**Fig. 1.** (a) Volume of 40-atom supercells as function of the average B-cation radius (a list of all supercells is given in table S1 in the SI; the radii for Fe<sup>3+/4+</sup> refer to iron in high-spin state). (b) Dop-O and Fe-O distances (averaged within the FeO<sub>6</sub> octahedron with largest distance to Dop in the respective cell) as function of the B-cation radius. Data for Ba<sub>8</sub>Fe<sub>8</sub>O<sub>24</sub> and Ba<sub>8</sub>Fe<sub>8</sub>O<sub>24</sub>H from [16]. The dashed lines are a guide for the eye only.

accommodate dopants and protons, symmetry restrictions need to be relaxed. The BaFeO<sub>3</sub> structure is then further modified by the lattice distortions around Dop<sub>Fe</sub><sup>•</sup> and OH<sub>O</sub><sup>•</sup>. Therefore, despite careful selection of starting geometries and crosschecking of the minimization procedure, it cannot completely be ruled out that some configurations still correspond to metastable states (local minima) rather than to the global energy minimum (for the respective Dop<sub>Fe</sub><sup>•</sup>-proton distance). Some energy variations are probably related to the fact that the distortion patterns within the supercells can develop in several closely related but not identical modes.

We used the climbing-image nudged elastic band method (CI-NEB [56,57]) for the calculations of proton migration barriers in 2 × 2 × 2 supercells. This size is consistent with our preceding and literature data on proton migration barriers in perovskites and suffices to extract the main differences between different configurations (NEB barriers for low-symmetry 4 × 4 × 2 cells with open-shell ions would be computationally much more demanding than e.g. for closed-shell BaZrO<sub>3</sub>), in particular since the dependence of total energy on the Dop...H distance largely agree for both cell sizes (Figs. 3,4). The number of images was 11 including the initial and final proton positions. During the NEB, the cell lattice parameters were kept fixed to the optimized values of the initial configuration (test calculations for undoped BaFeO<sub>3</sub> with full relaxation during NEB [16] indicate this is an acceptable approximation). The convergence parameters in the CI-NEB for the electronic and ionic relaxation were 10<sup>-5</sup> eV for energy and forces smaller than 10<sup>-2</sup> eV/Å. Since the proton transfer barriers are more or less asymmetric, we use the average of forward and backward barrier (“kinetically resolved barrier” KRA [58]) for further discussions.

### 3. Results and discussion

#### 3.1. Effect of dopants on volume and bond lengths

In BaFeO<sub>3</sub>, substitution of Fe on the perovskite’s B-site by more or less oversized Dop<sup>3+</sup> is expected to lead to changes in the molar volume as well as in Fe-O and Dop-O bond lengths. The volume of 40-atom supercells increases from Ba<sub>8</sub>Fe<sub>8</sub>O<sub>24</sub> to Ba<sub>8</sub>Fe<sub>8</sub>O<sub>24</sub>H because one Fe is (formally) reduced to Fe<sup>3+</sup> and one proton added to the cell (Fig. 1a). A similar cell volume is obtained for Ba<sub>8</sub>Fe<sub>7</sub>GaO<sub>24</sub>H and Ba<sub>8</sub>Fe<sub>7</sub>ScO<sub>24</sub>H cells (despite smaller/larger Ga<sup>3+</sup>/Sc<sup>3+</sup> radius compared to Fe<sup>3+</sup>), but with pronounced variation for cells with different proton position at given overall stoichiometry. For Ba<sub>8</sub>Fe<sub>7</sub>InO<sub>24</sub>H and Ba<sub>8</sub>Fe<sub>7</sub>YO<sub>24</sub>H, a significantly larger volume is found.

The Fe-O distances remain essentially constant (Fig. 1b), while the

Dop-O distances increase with dopant ion radii. However, this increase is less pronounced than expected from the Shannon radii (slope = 0.6 in Fig. 1b). This indicates that the Dop-O bonds (and correspondingly also the O-Fe bond in Dop-O-Fe connections) are under compressive strain. The consequences of this compression on the protonation properties are discussed in more detail in sect. 3.2. The volume increase from Ba<sub>8</sub>Fe<sub>8</sub>O<sub>24</sub>H to Ba<sub>8</sub>Fe<sub>7</sub>YO<sub>24</sub>H amounts to 2.8 %, while from the expanded Y-O length an increase of 4.5 % would be expected. This suggests that the oversize of DopO<sub>6</sub> octahedra can in part also be accommodated by reorientation of the Jahn-Teller distortion pattern of neighboring FeO<sub>6</sub> units.

#### 3.2. Energetics of proton sites

The total energy of protonated doped barium ferrate supercells with different proton-dopant configurations depends on several parameters. Since the relative charge of the dopant (Dop<sub>Fe</sub><sup>•</sup>) and the protonic defect OH<sub>O</sub><sup>•</sup> compared to the perfect lattice are negative and positive, there will be an electrostatic attraction between them. In addition to this, Dop<sub>Fe</sub><sup>•</sup> and OH<sub>O</sub><sup>•</sup> both lead to local lattice distortions. This makes certain configurations of OH<sub>O</sub><sup>•</sup> relative to the dopant more or less favourable, which may be subsumed under “elastic interaction”. The protonic defect needs suitable O...O distances to be well stabilized by hydrogen bond and to achieve a low-energy transition state for proton transfer. Fig. 2a illustrates the bonding situation around a proton. It is bound by a short covalent bond to O<sub>a</sub>, and forms a comparably strong hydrogen bond with typical distances in the range of 1.8–2.1 Å to O<sub>b</sub> (bold dashed line). I.e. O<sub>b</sub> is the hydrogen-bond acceptor, while O<sub>a</sub> has the role of the hydrogen-bond donor. While in many materials a proton forms only a single hydrogen bond, within the perovskite structure O<sub>c</sub> has an only moderately larger distance to the proton than O<sub>b</sub> (thin dashed line, H...O<sub>c</sub> distance 2.3–2.8 Å). This interaction is weaker than the shorter H...O<sub>b</sub> hydrogen bond, but at least for the shorter of the observed H...O<sub>c</sub> distances some interaction is still present (O<sub>c</sub> often also shows an inwards displacement similar as O<sub>b</sub> but with smaller magnitude). Thus, we address this H...O<sub>c</sub> distance still as a second, longer and weaker hydrogen bond (in line with BaZrO<sub>3</sub> electrolytes where also a second hydrogen bond is indicated [59]). A short O<sub>a</sub>...O<sub>b</sub> distance favors the formation of a short and strong H...O<sub>b</sub> hydrogen bond. However, in doped BaFeO<sub>3</sub> it does not suffice as a sole descriptor for a low-energy configuration; Fig. S1b,f,j,n illustrates that there is no clear correlation between the O...O distance and the energy of the specific configuration (relative to the lowest energy).

The hydrogen bond formation pulls the two O closer together

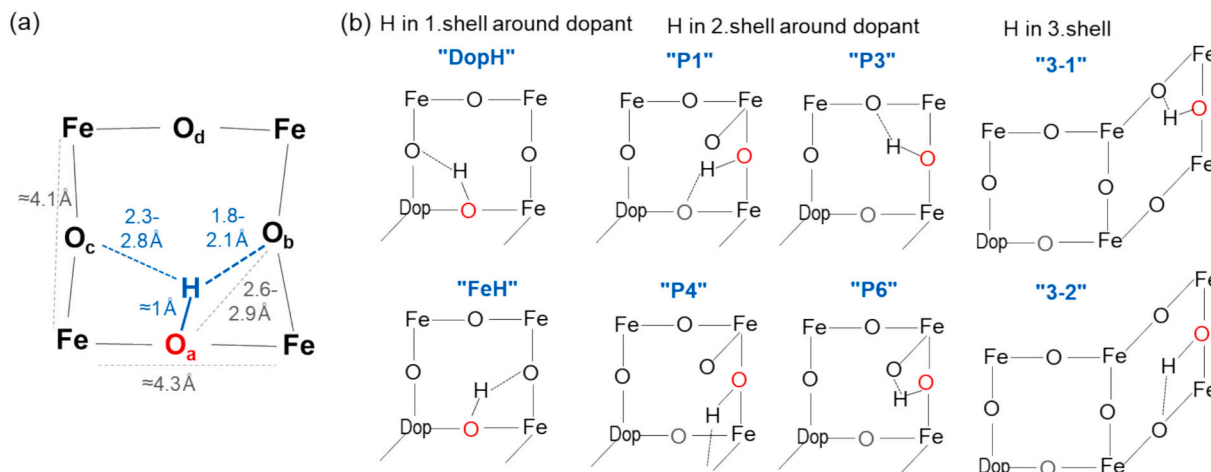


**Fig. 2.** (a) Bonding situation around a proton in BaFeO<sub>3</sub>, and relevant distances. (b) The unique proton positions in different shells around the Dop<sub>Fe</sub> in 40-atom 2 × 2 × 2 cells.

compared to the unprotonated situation. Since the OH has less negative charge than an unprotonated oxide ion, the distance between the neighboring Fe is increased. The two Fe-(OH) distances typically have different lengths: Either the shorter or the longer Fe-(OH) is located within the O-Fe-O-H...O quadrangle (table S1). Finally, the Fe-O bonds in barium ferrate perovskites exhibit a high degree of covalency [16,44], which is also sensitive to local distortions such as Fe-O-Fe buckling induced by oversized dopants [26]. Since the proton affinity of oxide

ions has been found to be generally closely related to the electronic structure of O (as expressed by the ionization potential, or by the O2p band centre) [16,60], it is expected that local changes in Fe-O bonding around the dopant will affect also the protonation propensity of the respective oxygen sites.

We will discuss the dependence of the total energy of the protonated supercells on proton-dopant distance here in the sequence of increasing dopant radius. For most dopants, results from both 40-atom

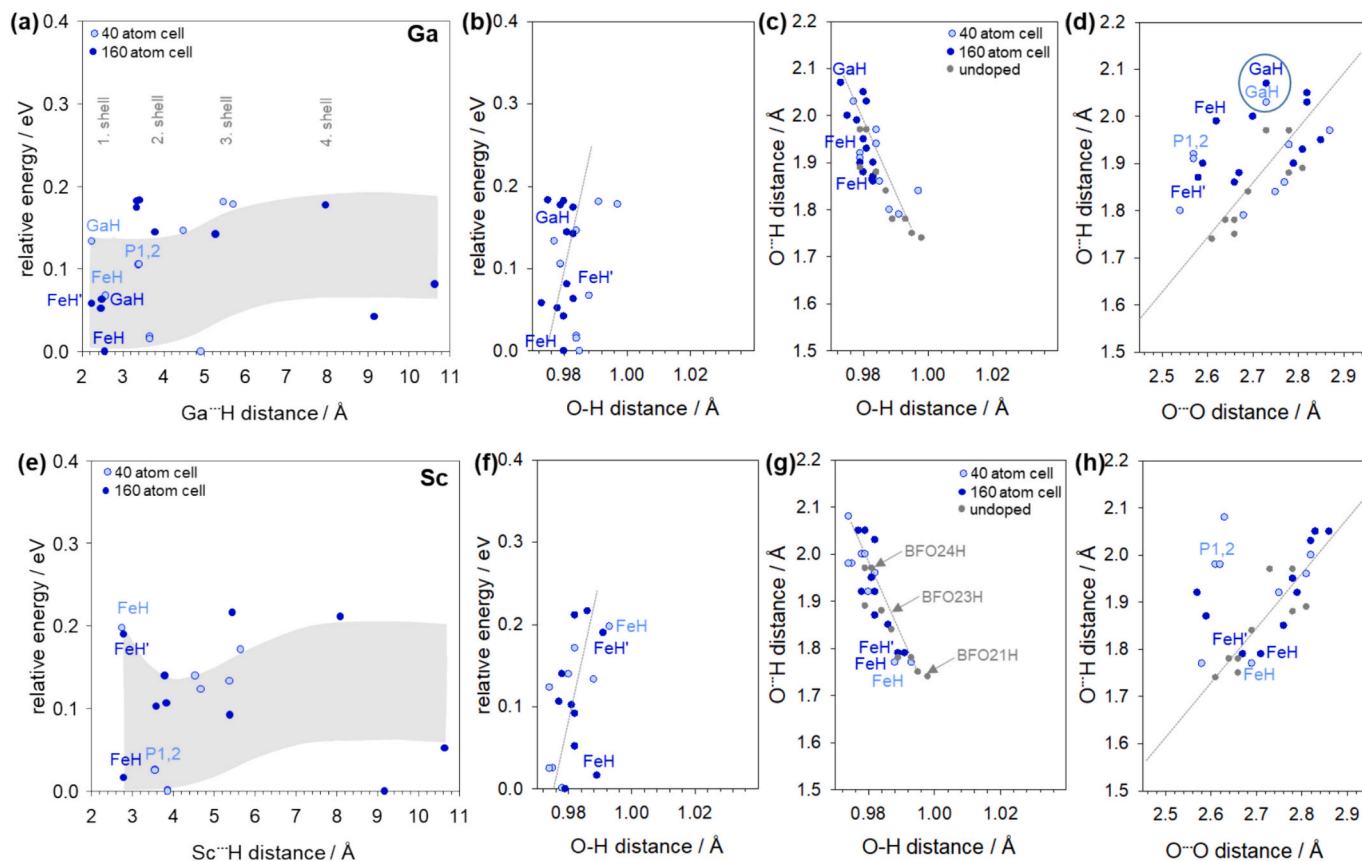


**Fig. 3.** (a,b,e,f) Relative energy as function of Ga- and Sc-proton distance and O-H bond length. The shaded area in (a,e) indicates the range of the potential energy. (c,d,g,h) Length of the short O<sub>b</sub>...H hydrogen bond as function of the O-H bond lengths, and of the O<sub>a</sub>...O<sub>b</sub> distance. The dashed straight lines are only a guide to the eye, but identical in the respective plots for Ga,Sc,In,Y. The grey data points give the respective distances for undoped BaFeO<sub>3-δ</sub> with different oxygen deficiencies [16] (BFO24H = Ba<sub>8</sub>Fe<sub>8</sub>O<sub>24</sub>H cell etc.).

(Ba<sub>8</sub>Fe<sub>7</sub>DopO<sub>24</sub>H, corresponding to 12 % doping, Fig. 2b) and 160 atom (Ba<sub>32</sub>Fe<sub>31</sub>DopO<sub>96</sub>H, 4 × 4 × 2 cell corresponding to 3 % doping) supercells are reported. In actual triple-conducting materials, dopant concentrations up to approx. 20 % are present [2,7,14], thus defect interactions may be even stronger and no “undistorted” BaFeO<sub>3</sub> remains between them.

### 3.2.1. Ga- and Sc-doped BaFeO<sub>3</sub>

The dopants Ga<sup>3+</sup> (0.62 Å) and Sc<sup>3+</sup> (0.74 Å) are slightly to moderately oversized relative to iron (Fe<sup>3+</sup> 0.605 Å and Fe<sup>4+</sup> 0.585 Å; all radii for 6-fold coordination and high-spin state [37]), and are therefore discussed together. Fig. 3a,e shows the “potential energy curve” of the supercells as function of the Dop<sub>Fe</sub>-proton distance, i.e. the energy relative to the lowest total energy for 40-atom and 160-atom cells, respectively. This relative energy can also be regarded as the “proton-dopant interaction energy”, although it also comprises indirect contributions (e.g. from distortions of FeO<sub>6</sub> octahedra). The Dop<sub>Fe</sub>-proton distance may not suffice as sole descriptor for the relative energy of protonation sites; the orientation of O-H and O···H bonds may further modify the energy landscape. Correspondingly, instead of a single potential energy curve, Fig. 3a,e and Fig. 4a,e give a range with a width of ≈0.1 eV (shaded area) to describe the energy of protonation sites as function of Dop<sub>Fe</sub>-proton distance. The results from the smaller and larger supercells agree within this range.

For both Ga<sup>3+</sup> and Sc<sup>3+</sup>, the energy variation with the proton position remains within a range of 0.2 eV. In the 40-atom cells, O in the first coordination shell around the Dop<sub>Fe</sub> (Fig. 2b) does not represent the energy minimum, as it would be expected from a simplistic picture dominated by electrostatic defect interaction only. This indicates that elastic interactions and modified local structure around the Dop<sub>Fe</sub> are also important. For Ga<sup>3+</sup> as the smallest dopant, stable proton positions

in the first shell around Ga<sup>3+</sup> can be obtained in both the “GaH” (hydrogen bond pointing towards Ga) and “FeH” configuration (O···H pointing towards Fe, cf. Fig. 2b). However, for both supercell sizes the energy for “GaH” is higher than for “FeH”. This can be attributed to the average Ga-O bond length of 2.07 Å being moderately larger than the average Fe-O distance (2.02 Å, Fig. 1b). The corresponding larger O···O distance destabilizes the hydrogen bonding (long O···H, marked in Fig. 3d) and leads to an increased total energy. The FeH configuration, for which the hydrogen bond occurs along the shorter FeO<sub>6</sub> octahedron edge, has a lower energy. In the 160-atom supercell, which allows for more relaxation, FeH with the proton in the first shell around Ga<sub>Fe</sub> represents the energy minimum (the energy of the FeH' configuration in which the FeOHFe connection is oriented along the non-expanded direction is higher).

For Sc<sup>3+</sup>, the larger Sc-O length of 2.14 Å disfavours the ScH configuration so much that it could not be converged any more in the energy minimization. The energy of the first shell FeH configuration represents the energy minimum for 160-atom cells. FeH' is not only higher than FeH, but also higher than most second shell configurations. This trend of less favourable total energy for configurations which do not allow for optimum relaxation around the proton (caused by proximity to oversized dopant and/or FeOHFe oriented along the non-expanded direction of the supercell) will become even stronger for the larger dopants discussed below.

Some more details of the bonding situation around the proton are depicted in Fig. 3b-d,f-h. Fig. 3b,f shows the relative energy as function of the O-H covalent bond length. This length remains in a narrow range of 0.974–0.997 Å, with a tendency of higher energy for larger O-H distances (i.e. weaker O-H bonds). Correlations between different distances around protons have been observed in literature (e.g. [61–64]), and respective relations are observed also here. The correlation of the O<sub>b</sub>···H

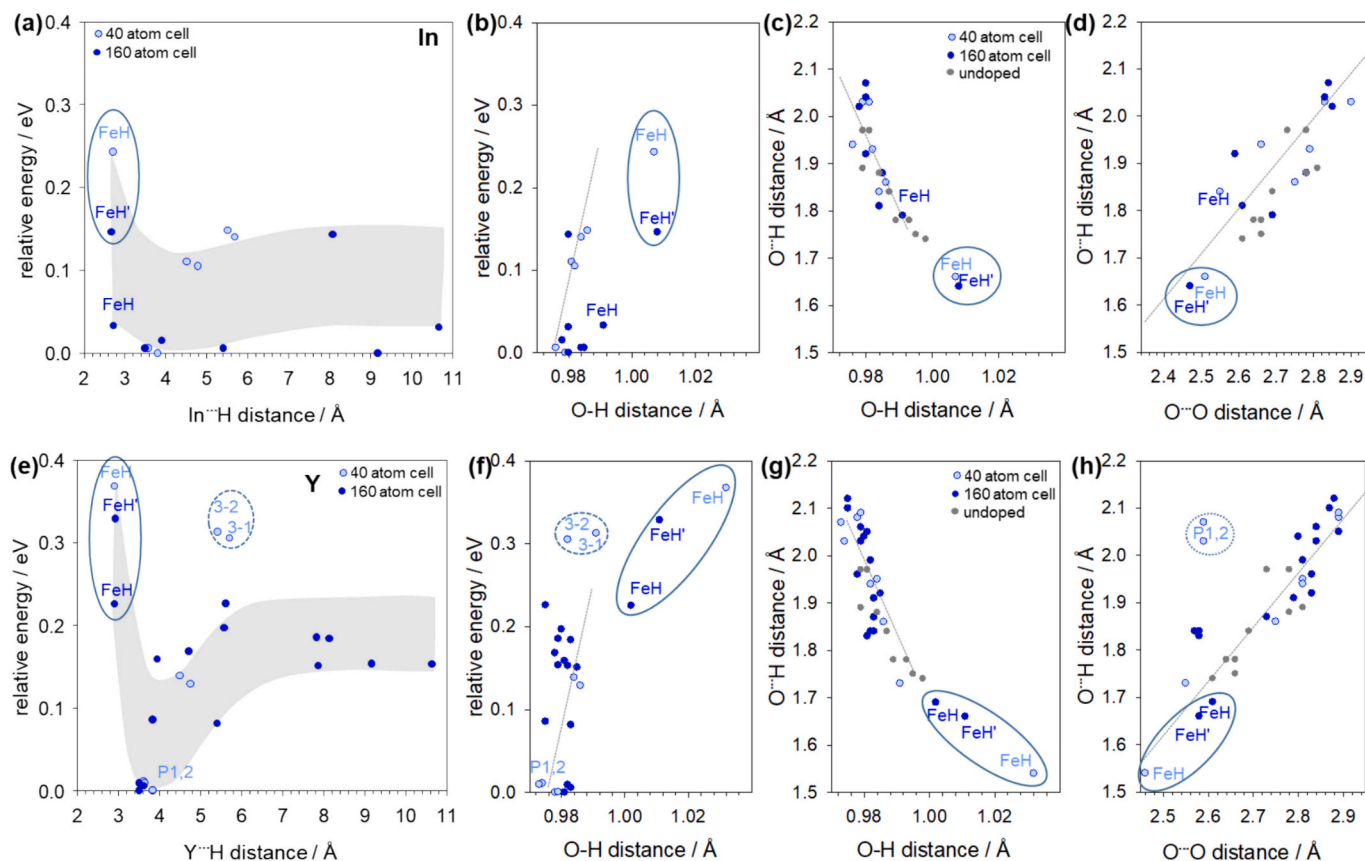


**Fig. 4.** (a,b,e,f) Relative energy as function of In- and Y-proton distance and O-H bond length. (c,d,g,h) Length of O<sub>b</sub>···H hydrogen bond as function of O-H bond length and O<sub>a</sub>···O<sub>b</sub> distance, the dashed straight lines are the same as in Fig. 3.

length of the shorter of the two hydrogen bonds with the covalent O-H bond length is displayed in Fig. 3c,g. For both  $\text{Ga}^{3+}$  and  $\text{Sc}^{3+}$  the data from the doped cells span approximately the same range as the respective data for undoped  $\text{BaFeO}_{3-\delta}$  (grey symbols, data from [16]; in these cells one or several Fe are in  $3+$  oxidation state). The data roughly follow a correlation that a shorter covalent O-H bond typically leads to a longer  $\text{O}\cdots\text{H}$  hydrogen bond. This can be attributed to the fact that the proton is located between two O with an  $\text{O}\cdots\text{O}$  distance largely determined by the  $\text{FeO}_6$  and  $\text{DopO}_6$  octahedra. The repulsion of the proton to the central cation of this octahedron results in an outward bending of the  $\text{O-H}\cdots\text{O}$  connection, cf. Fig. 2a, Fig. 6, Fig. S1).

Fig. 3d,h shows the  $\text{O}\cdots\text{H}$  hydrogen bond length as function of the  $\text{O}\cdots\text{O}$  distance. The main trend that larger  $\text{O}\cdots\text{O}$  distances lead also to larger  $\text{O}\cdots\text{H}$  hydrogen bonds reflect the fact that the proton is situated in-between the two oxide ions. For both  $\text{Ga}^{3+}$  and  $\text{Sc}^{3+}$  some configurations slightly deviate, having rather long  $\text{O}\cdots\text{H}$  despite short  $\text{O}\cdots\text{O}$  distances. These are mainly proton positions in the first and second shell, and the oxide ions acting as bonding partners for the hydrogen bond have comparably short Fe-O bonds (indicating increased covalency) which makes them less favourable for hydrogen bonding interactions. However, these proton configurations often have short covalent O-H bonds (Fig. 3c,g) which explains why the overall energy remains comparably low. Further correlations of the local bonding geometry are shown in the SI Fig. S1.

Overall, the Ga- and Sc-doped cells show only moderate energy variations for the different proton configurations, with lower energies in the first and/or second shell compared to long Dop-H distances.

### 3.2.2. In- and Y-doped $\text{BaFeO}_3$

The dopants  $\text{In}^{3+}$  (0.80 Å) and  $\text{Y}^{3+}$  (0.90 Å) are strongly oversized relative to iron, which strongly modifies the energy landscape and leads to much larger energy variations as compared to  $\text{Ga}^{3+}$  and  $\text{Sc}^{3+}$ . Fig. 4a,e shows the dependence of the relative energy on Dop $\cdots\text{H}$  distance. Similar to Sc, “DopH” configurations with the hydrogen bond oriented towards the Dop $^{3+}$  could not be converged, which can be related to the long In-O (2.18 Å) and Y-O (2.23 Å) and correspondingly very expanded  $\text{O}\cdots\text{O}$  distances that prohibit efficient hydrogen bonding.

FeH and FeH' proton positions in the first coordination shell are not only higher in energy than the minimum (which is found for the second shell), but are also higher than the values for large distances (3./4. shell). This means that protons are actually repelled from the first shell around  $\text{Y}'_{\text{Fe}}$  (and to smaller degree also from  $\text{Sc}'_{\text{Fe}}$ ). This is in stark contrast to proton-dopant interaction seen in electrolyte-type  $\text{Ba}(\text{Ce,Zr})\text{O}_3$  perovskites, which exhibit an energy minimum for protons in the first - and sometimes also second - coordination shell around the B-site dopant (e.g. [19–23,25]).

At a distance of  $\approx 5.5$  Å to  $\text{Y}'_{\text{Fe}}$  (dotted circles in Fig. 4e-h) the protons already feel the effect of the oversized dopant in the next cell; it is more pronounced for the very oversized  $\text{Y}^{3+}$  than for  $\text{Ga}^{3+}$ ,  $\text{Sc}^{3+}$ , and  $\text{In}^{3+}$ . For  $\text{Y}^{3+}$ , there are also some specific proton configurations in the second shell with rather long  $\text{O}\cdots\text{H}$  despite short  $\text{O}\cdots\text{O}$  distances (P1,2; dotted circles in Fig. 4 h and S1p).

The strong local distortions caused by  $\text{In}'_{\text{Fe}}$  and particularly by  $\text{Y}'_{\text{Fe}}$  are well visible in Fig. 4b-d,f-h. The values of O-H,  $\text{O}_b\cdots\text{H}$  and  $\text{O}_a\cdots\text{O}_b$  distances exceed the range found for undoped and Ga,Sc-doped  $\text{BaFeO}_3$ . Fig. 4b,f demonstrates that protons in the first shell (marked by blue circle) exhibit exceptionally long O-H bonds. The corresponding  $\text{O}_b\cdots\text{H}$  hydrogen bonds become shorter than 1.7 Å, but apparently this does not supply sufficient stabilization to obtain a low total energy. The data of the first shell configurations for Y in Fig. 4 g strongly deviate from the trend line of the other configurations, and the slope of  $\text{O}_b\cdots\text{H}$  versus O-H bond length changes. To follow the overall trend and obtain lower energies,  $\text{O}_b\cdots\text{H}$  for FeH and FeH' should be even shorter, which is, however, prevented by the achievable  $\text{O}\cdots\text{O}$  distances. This repulsive behaviour holds for the FeH configuration in the 40-atom cell, as well as

for the FeH and FeH' configurations (with different orientation of Y-OH-Fe relative to the expanded cell directions) of the 160-atom cell.

For the interpretation of the proton-repulsive behaviour in the first shell — despite electrostatic attraction of oppositely charged point defects — let us focus on the Y dopant, where the effect is strongest. Already in the unprotonated state Y is significantly oversized relative to Fe in the  $\text{BaFeO}_3$  matrix. The increase in Y-O bond length of 0.2 Å compared to Fe-O is less than expected from the ionic radii (Fig. 1b), and the Fe $\cdots\text{Y}$  distance expands only by  $\approx 0.1$  Å (i.e. the Fe-O adjacent to Y are also compressed).

This situation with local compressive strain is further aggravated by the presence of protons. Replacing an oxide ion by a singly charged hydroxide ion leads to an expansion of Fe-(OH), Dop-(OH) and Fe $\cdots\text{Dop}$  distances, as indicated in Fig. 5. Far from the dopant, the Fe $\cdots\text{Fe}$  distance increases by 0.3 Å from 4.0 Å to  $\approx 4.3$  Å upon protonation (Fig. 5a), and close to moderately oversized Sc the expansion amounts to  $\approx 0.5$  Å (Fig. 5b). However, for Y the increase relative to the unprotonated case reaches only  $\approx 0.4$  Å (Fig. 5c; unprotonated Fe $\cdots\text{Y}$  is 4.08 Å) because the unprotonated region opposite to the OH is already under strong compressive strain, i.e. the proton environment cannot relax as much as desired. This additional strain increases the total energy in particular for the proton in the first shell around Y. Also the decreased OFeO angles in the Fe-O-H $\cdots\text{O}$ -Fe polygon resulting from Fe being pushed away from Y contribute to this energy increase.

A second consequence of the large  $\text{Y}^{3+}$  size is that the corresponding long  $\text{O}\cdots\text{O}$  distances at the edges of the  $\text{YO}_6$  octahedron make the formation of the second hydrogen bond  $\text{O}_c\cdots\text{H}$  unfavourable for a proton in the first shell. This can be recognized in Fig. 5c and S1o; the  $\text{O}_c\cdots\text{H}$  bond length becomes exceptionally long. This leads to a shortening of the  $\text{O}_b\cdots\text{H}$  hydrogen bond, and a comparably short  $\text{O}_a\cdots\text{O}_b$  distance along the  $\text{FeO}_6$  octahedron edge. Furthermore, for the FeH and FeH' configurations with the proton in the first shell around Y, the covalent O-H bond is significantly expanded (Fig. 4g). Overall the large distortions from an optimum proton bonding geometry are detrimental for the total energy. The bonding situation is more relaxed when the proton is in the second shell around the dopant, as shown by the exemplary configurations in Fig. 5d,e. In these configurations also the H $\cdots\text{O}_c$  hydrogen bond is comparably short and can contribute to the stabilization.

In addition one might expect that pronounced lattice distortions also affect the electronic structure. The shortening of Fe-O bonds — owing to the compressive strain exerted by Y in Y-O-Fe connections (Figs. 5c, S2c) — typically correspond to increased covalency. This is expected to decrease the basicity of the oxide ion, and the proton affinity of oxide ions is sensitive to this [16,60]. However, the fact that the increased total energy for protons in the first shell around strongly oversized dopants comprises the direct effects of distortions on bonding geometries as well as indirect effects via modified energy levels of various oxide ions makes such an analysis hardly tractable.

In summary, we find a repulsive behaviour for protons in the first shell for strongly oversized  $\text{In}^{3+}$ , and even more pronounced for the very strongly oversized  $\text{Y}^{3+}$ , and an energy minimum (trapping zone) in the second shell which is lower by 0.1–0.2 eV compared to protons at large distance from the Dop $^{3+}$ . This repulsive effect is significantly increased by the actual presence of protons in the first shell. The finding of a repulsive region around  $\text{Y}^{3+}$  is in line with the experimental observation from thermogravimetry that very oversized dopants with a typical concentration of 20 % on the Fe site do not necessarily yield the highest proton uptake [65].

### 3.3. Proton migration barriers

The long-range proton transport in perovskite oxides comprises different elementary steps: (i) reorientation (e.g. between configurations P1 and P3), (ii) rotation (e.g. between P1 and P4), and (iii) transfer (e.g. from FeH to P1, or P3 to P3 but interchanging covalent and hydrogen bond). In the reorientation and rotation steps (i,ii), the short and strong

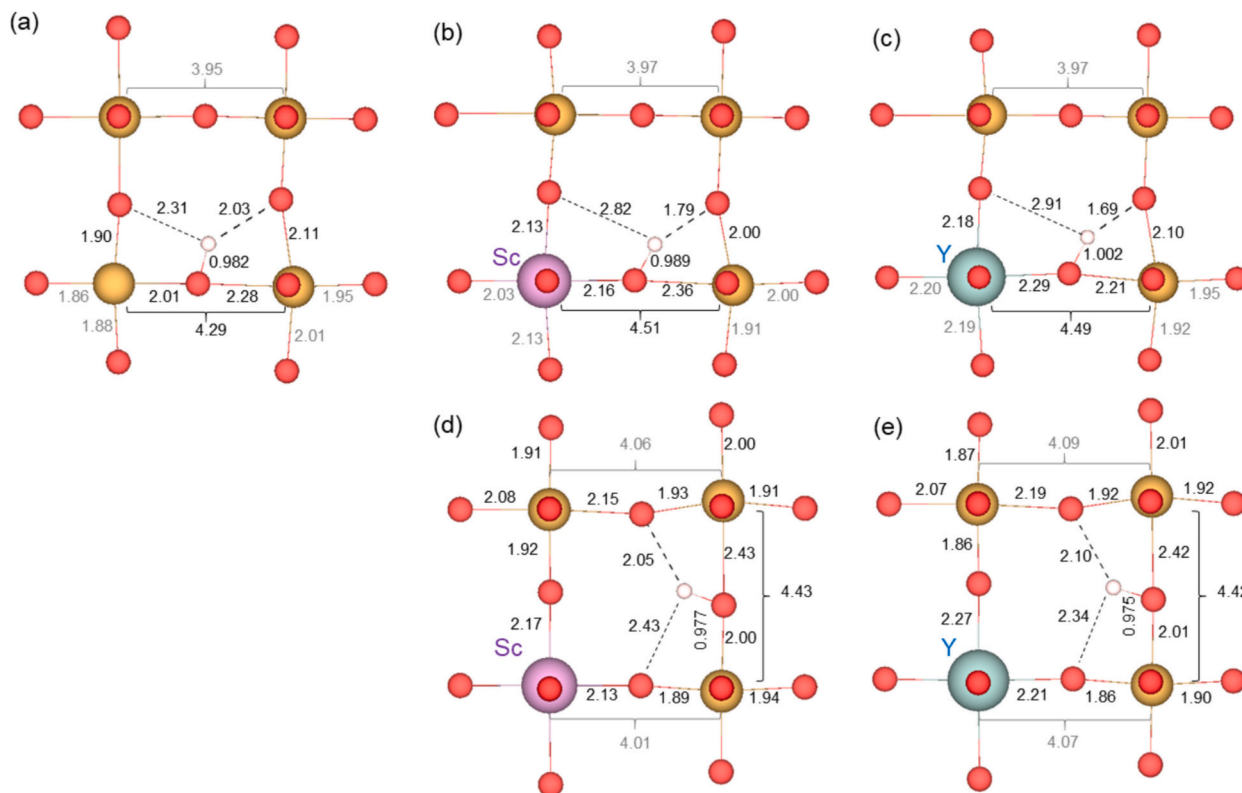


**Fig. 5.** Local geometry around the proton in 160-atom cells, distances in Å. (a) Far away from dopant, (b,c) proton in first shell around  $\text{Sc}^{3+}$ ,  $\text{Y}^{3+}$  (FeH config.); (d,e) proton in second shell around  $\text{Sc}^{3+}$ ,  $\text{Y}^{3+}$  (P3 config.). The respective plot for 40-atom cells is given in Fig. S2.

O-H covalent bond remains intact while the weaker hydrogen bonds rearrange. The O-H covalent bond is broken only in the transfer step. Correspondingly, this step has the lowest rate and becomes limiting. This has been found for electrolyte-type  $\text{Ba}(\text{Ce,Zr})\text{O}_3$  perovskites [22,25,66–68], as well as for undoped  $\text{BaFeO}_3$  [16]. Also ab-initio molecular dynamics yields significantly higher rate for reorientation and rotation compared to transfer in  $\text{BaFeO}_3$  [69]. Therefore, we concentrate here on the effect of B-site dopants for the proton transfer step.

Fig. 6a shows an exemplary proton transfer trajectory of Sc-doped  $\text{BaFeO}_3$  with equivalent initial and final state in the second and third shell around  $\text{Sc}^{3+}$ . Key features of the proton transfer show up when

analysing the evolution of  $\text{O}_a\text{-H}$ ,  $\text{O}_b\cdots\text{H}$ , and  $\text{O}_a\cdots\text{O}_b$  distances. The bottom plot demonstrates that the transfer occurs in two stages, similar as in electrolyte-type perovskites [13]. In first four steps along the reaction coordinate, the  $\text{H-O}_a$  covalent bond length remains almost constant, while the  $\text{O}\cdots\text{O}$  distance and correspondingly also the length of the  $\text{H-O}_b$  hydrogen bond (dashed red line) decrease strongly by more than 0.3 Å. Only in the subsequent steps the actual proton transfer occurs, with the former  $\text{O}\cdots\text{H}$  now becoming the new covalent O-H bond. These two stages can also be recognized in plots of relative energy versus  $\text{O}\cdots\text{O}$  distance (Fig. SI3–6), which exhibit a much steeper slope for the actual transfer (1.0–1.3 eV/Å) than for the initial  $\text{O}\cdots\text{O}$  approach (0.2–0.35 eV/Å). Since

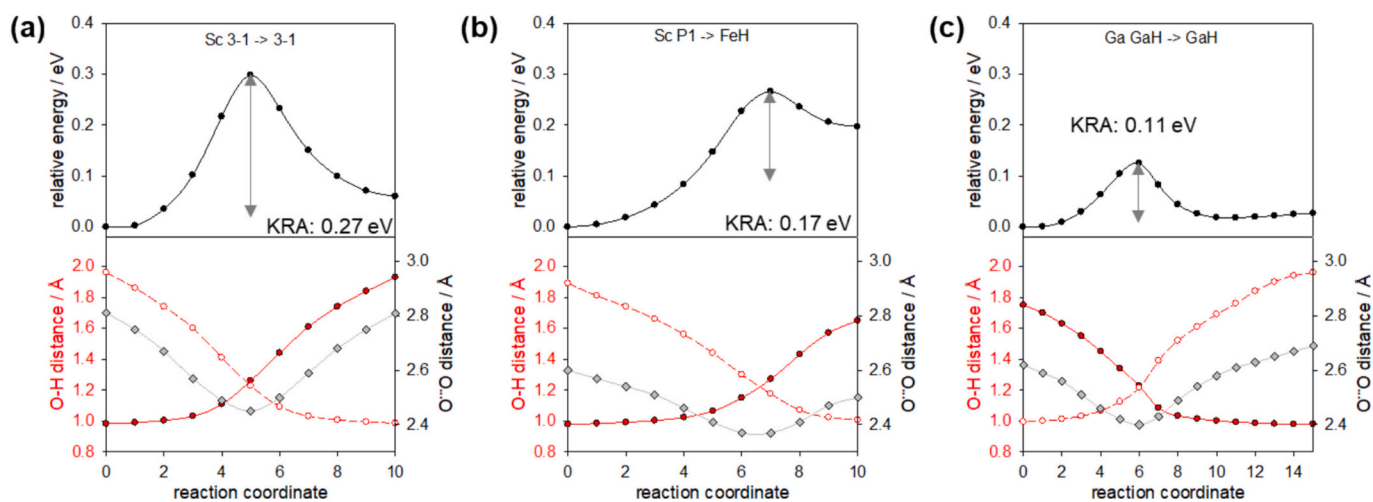


**Fig. 6.** (a) Exemplary proton transfer trajectories (40-atom cells), the bottom parts show the evolution of  $\text{H-O}_a$  distance (solid red line; distance to initial O),  $\text{H-O}_b$  (dashed red line; distance to final O), and  $\text{O}_a\cdots\text{O}_b$  distance (grey line) during the transfer. (a,b) Proton transfers in third and second shell of Sc-doped  $\text{BaFeO}_3$ , (c) proton transfer around  $\text{Ga}^{3+}$ . (For interpretation of the references to colour in this figure legend, the reader is referred to the web version of this article.)

the O...O approach is prerequisite for the actual proton transfer, modifications of the respective phonon frequencies will also affect the proton transfer rates. When initial and final state are nonequivalent (Fig. 6b) the barrier becomes strongly asymmetric, and the transition state is shifted from the middle of the reaction coordinate to an image closer to the high-energy state (but still the points of two equal O...H distances and highest energy approximately coincide). The proton transfer in the first shell around  $\text{Ga}^{3+}$  along a  $\text{GaO}_6$  octahedron edge (Fig. 6c) follows the same mechanism, but starts already with a comparably short O...O distance and exhibits a significantly lower barrier. (For the larger dopants no proton transfer path along an  $\text{DopO}_6$  edge could be obtained). Further proton trajectories for Sc and the other dopants are shown in Fig. SI3–6. Transfers between different coordination shells around the dopant have larger energy differences between initial and final state, thus the barriers are more asymmetric.

Similar as for undoped  $\text{BaFeO}_3$  without and with oxygen deficiency [16], we obtain a correlation of the KRA barrier heights with the initial/final O-H bond length and O...O distance. Lower barriers are related to longer, i.e. weaker, O-H bonds, and shorter O...O distances that require less O...O approach before the actual proton transfer. Fig. 7a shows that the barriers of doped  $\text{BaFeO}_3$  (coloured diamonds) follow the same correlation as for undoped  $\text{BaFeO}_{3.5}$  (grey circles) [16]. The grey plane fitted with the full data set yields a very similar dependence on O...H and O...O distances as the fit for undoped  $\text{BaFeO}_{3.5}$  only. The advantage of such a correlation based on initial/final state geometries is that it allows for barrier prediction even without actual NEB calculation.

An even slightly better correlation is found when instead of the absolute O-H and O...O distances the difference of O-H and O...O distances between initial/final state and transition state are used (Fig. 7b). While the presence of dopants leads to a larger range of  $\Delta\text{O-H}$  and  $\Delta\text{O...O}$  (in particular large  $\Delta\text{O...O}$  combined with short  $\Delta\text{O-H}$ ), still an overall correlation of these two quantities with the barrier height holds for undoped and doped  $\text{BaFeO}_3$ . This emphasizes that these parameters indeed reflect the decisive physical processes during the two-stage proton transfer. The dependence of the barrier height on  $\Delta\text{O-H}$  is larger than on  $\Delta\text{O...O}$ , but one has to keep in mind that  $\Delta\text{O-H}$  represents the change of the O-H covalent bond length which naturally has a higher force constant than the O...O distance.

We need to mention that the equation of the fitted grey plane in Fig. 7b is not identical to that for undoped barium ferrate. The  $\text{BaFeO}_{3.5}$

data in Fig. 9c in [16] closely follow a line, i.e. a rotation around this line has little influence on the fit quality. Several of the additional data points for doped  $\text{BaFeO}_3$  deviate from this line, and correspondingly a modified equation of the fitting plane yields a better (and numerically much more robust) correlation. Those data of doped  $\text{BaFeO}_3$  which are located close to the undoped  $\text{BaFeO}_{3.5}$  points are often barriers with a large H...Dop distance, the barriers situated in the left hind region tend to stem from barriers for which the proton is closer to the  $\text{Dop}^{3+}$  and more affected by respective lattice distortions.

In both Fig. 7a and b the proton transfer along an edge of the  $\text{GaO}_6$  octahedron (dashed pink box) significantly deviates from the overall correlation. The barrier of 0.11 eV is much smaller than expected for the respective O...H and O...O distances and their changes. This is the only barrier in the present investigation where the proton migrates along the edge of an octahedron with (formally) a 3+ cation in the centre. A similar situation is met for  $\text{Y}^{3+}$  in  $\text{BaZrO}_3$ , where also a decreased barrier is found for the proton transfer along the  $\text{DopO}_6$  edge [22,25]. The common aspect is that the proton migrates around an  $\text{Dop}^{3+}$  dopant that is only slightly oversized ( $\text{Y}^{3+}$  in  $\text{BaZrO}_3$ ,  $\text{Ga}^{3+}$  in  $\text{BaFeO}_3$ ). The decreased barrier can tentatively be attributed to a decreased repulsion between the proton in the transition state (when the proton is least screened by immersion into the electron cloud of oxide ions) and the central cation, and possibly also to softer O...O phonons around such a  $\text{Dop}^{3+}$ . For larger dopants the detrimental effects of the locally expanded  $\text{Dop-O}$  and O...O distances outweigh this advantage.

The data in Fig. 7 indicate that the ranges of barriers for the different dopants overlap strongly, i.e. there is no simple overall correlation between dopant radius and proton transfer barrier. The varying local geometry of the respective specific configurations is important; in particular the initial O...O distance and its change  $\Delta\text{O...O}$  up to the transition state. Within the present investigation, the largest barrier of 0.32 eV is found in the second shell of Y-doped  $\text{BaFeO}_3$  with an initial  $\text{O}_a\cdots\text{O}_b$  distance of 2.89 Å. The combined effect of modified proton barriers and varying initial/final state energies on the proton mobility in doped  $\text{BaFeO}_3$  is discussed in the next section.

### 3.4. Concluding discussion

Before discussing the energy landscape for long-range proton transport in doped  $\text{BaFeO}_3$ , let us recap the situation in  $\text{BaZrO}_3$  doped with

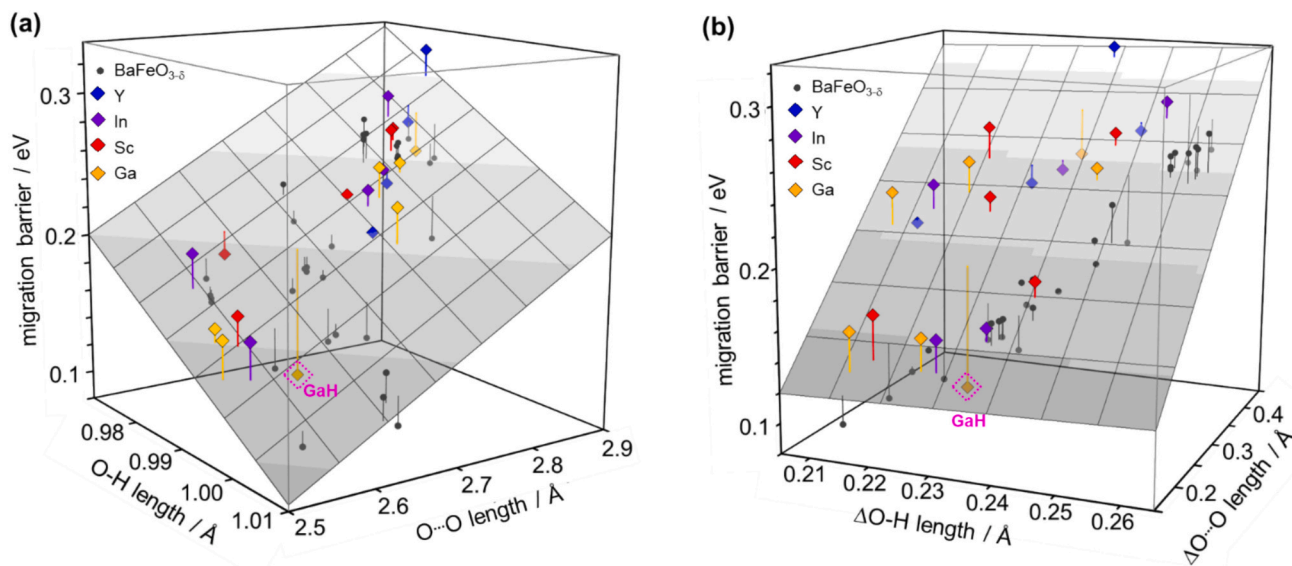


Fig. 7. Proton transfer barriers (average of forward and backward direction (KRA)) in undoped and doped  $\text{BaFeO}_3$  (a) as function of O-H and  $\text{O}_a\cdots\text{O}_b$  distance (averaged over initial/final state); (b) as function of the O-H and O...O distance changes between initial/final and transition state. Data for undoped  $\text{BaFeO}_{3.5}$  from [16].



$\text{Sc}^{3+}$  and  $\text{Y}^{3+}$ , representing a size-matched and a moderately oversized dopant, based on literature data ([22], GGA-PW functional). It has to be noted that proton trapping energies and migration barriers in  $\text{BaZrO}_3$  depend sensitively on technical details (supercell size, exchange-correlation functional, charge compensation, size corrections...) [70]. Fortunately, the relative trends of site energies and barriers remain consistent, even when the absolute values differ perceptibly (e.g. for Y- $\text{BaZrO}_3$  in [22,25]). For  $\text{Sc}^{3+}$  without size mismatch, protons are stabilized only in the first shell relative to large Dop-H distances (blue area in Fig. 8a). Owing to decreased repulsion in the transition state to the 3+ cation, the barrier is decreased in this shell, but transport without the need for de-trapping would be achieved only for very high  $\text{Sc}^{3+}$  concentration, as recently realized experimentally [71]. For low Sc concentrations, also the second shell protons positions with higher energy need to be included to form a long-range transport path (indicated by the hatched area in Fig. 8a; this decreases the effective mobility).

In contrast, for  $\text{Y}^{3+}$  which is moderately oversized relative to  $\text{Zr}^{4+}$ , both first and second shell exhibit a stabilization (but less than for  $\text{Sc}^{3+}$ ) with comparable stabilization energies [22–25,59]. Even for larger dopants in  $\text{BaZrO}_3$  such as  $\text{Gd}^{3+}$  or  $\text{Nd}^{3+}$  (0.94 Å and 0.98 Å, but the size difference to  $\text{Zr}^{4+}$  is still less than for  $\text{Y}^{3+}$  to  $\text{Fe}^{3+/4+}$  in  $\text{BaFeO}_3$ ) the first shell is attractive [22,24,72]. The extended trapping zones begin to overlap already at moderate Y concentrations ( $\approx 20\%$ ). Together with

the decreased barrier in the first shell this allows for fast proton transport [25]. This behaviour is in contrast to the interaction of  $\text{Y}^{3+}$  and  $\text{V}_\text{O}^\bullet$  in  $\text{BaZrO}_3$ : while the  $\text{V}_\text{O}^\bullet$  trapping energy has a similar trend (lowered energy in first and second shell around Y) the migration barrier of oxide ions is increased in the first shell [73].

Fig. 8b illustrates that the effect of  $\text{Sc}^{3+}$  and  $\text{Y}^{3+}$  in the  $\text{BaFeO}_3$  matrix is completely different. The difference is that relative to Fe in the  $\text{BaFeO}_3$  matrix,  $\text{Sc}^{3+}$  is moderately and  $\text{Y}^{3+}$  now very strongly oversized (cf. sect. 3.2). This makes the first shell slightly (for some  $\text{Sc}^{3+}$  configurations) or strongly ( $\text{Y}^{3+}$ ) unfavourable for protonation, not only relative to the lowest-energy position but also relative to the non-interacting configuration (large proton-dopant distances). Instead of being a proton trapping site as in  $\text{Ba}(\text{Ce},\text{Zr})\text{O}_3$  electrolytes, the first shell in Y-doped  $\text{BaFeO}_3$  is a repulsion zone. This represents a fundamental difference, because for elevated dopant concentrations an overlap of such exclusion zones can largely hinder or even block long-range proton transport.

For less oversized dopants the character of the first shell depends on the possibilities for geometry relaxation; in the 160-atom cells the energy of FeH configuration with the proton in the first shell is close to the energy minimum. A DopH configuration (proton in the first shell with hydrogen bonding along the  $\text{DopO}_6$  octahedron) could be obtained only for the smallest dopant,  $\text{Ga}^{3+}$ . It is higher in energy than the FeH configuration, but in the large cells still close to the overall energy

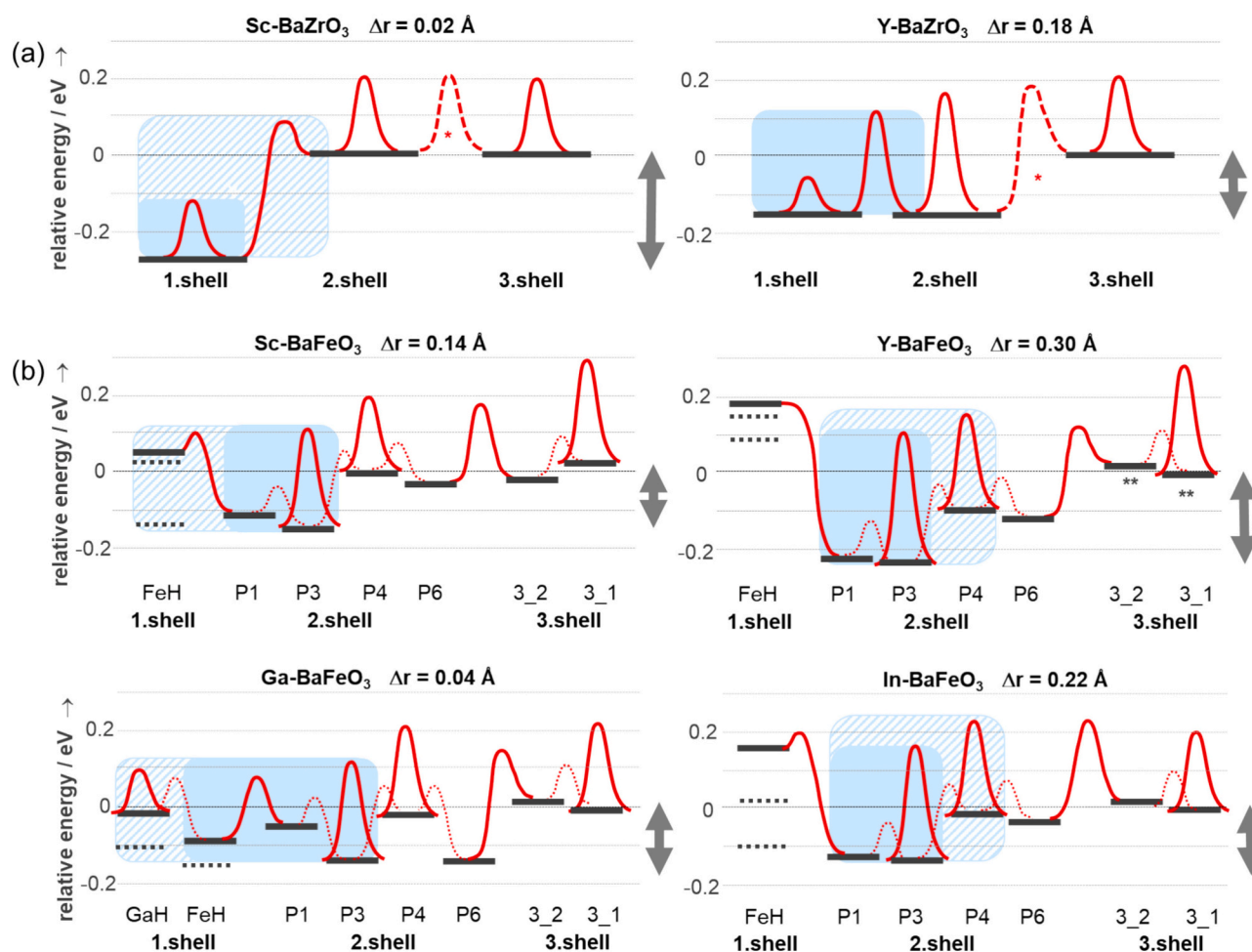


**Fig. 8.** (a) Sketch of proton site energies in first to third shell around  $\text{Sc}^{3+}$  and  $\text{Y}^{3+}$  in  $\text{BaZrO}_3$ , and respective proton transfer barriers (the dashed barriers are estimations as they were not calculated in the original reference) [22]. (b) Sketch of proton site energies in doped  $\text{BaFeO}_3$ , and respective proton transfer barriers in 40-atom cells (the levels marked by asterisks are adjusted to remove the spurious interaction with next Y cf. Fig. 4e; the grey dotted lines give the levels for respective 160-atom cells). The dotted curves indicate estimated reorientation barriers.  $\Delta r$  is the difference between host B-site cation ( $\text{Zr}^{4+}$ ,  $\text{Fe}^{4+}$ ) and  $\text{Dop}^{3+}$  Shannon radii. The light blue area indicates the trapping zone; if additional proton positions or barriers are required for long-range transport at 12 % dopant concentration they are indicated by the additional hatched area. (For interpretation of the references to colour in this figure legend, the reader is referred to the web version of this article.)

minimum.

Only for Ga a proton transfer trajectory within the first shell could be obtained, which features a particularly small barrier. The combination of an extended trapping zone comprising the second shell and at least some configurations in the first shell with comparably low barriers in this zone is expected to allow for a high proton mobility. A rough schematic consideration in Fig. S7 suggests that already a dopant concentration of 12.5 % suffices for a percolating low-barrier path. However, using only  $\text{Ga}^{3+}$  as dopant will probably not yield highest degrees of hydration, as indicated by the relation between proton uptake and dopant ion radius [65].

Sc presents a different situation. The second and some configurations from the first shell form an extended trapping zone, but ScH-ScH transfers within the  $\text{DopO}_6$  octahedron are not feasible. This limits the number of percolating paths, as indicated in the sketch in Fig. S8. Still for 12.5 % Sc long-range transport with comparably low barriers is expected, but at higher Sc concentration the unavailability of ScH-ScH transfers becomes more and more detrimental.

For In and Y, the barriers  $\text{FeH} \rightarrow \text{P1}$  towards the second shell are very asymmetric (Fig. 8b). The transfer barriers within the second shell are comparable or larger than within the third shell. Correspondingly, even if the second-shell trapping zones would overlap and percolate at sufficiently high dopant content, this would not yield a particularly high proton mobility. The barriers for Y in the third shell are still higher than for undoped  $\text{BaFeO}_3$  (average value 0.22 eV [16]); this is most probably related to the fact that the barriers in the 40-atom cells are still sensitive to dopant-induced lattice distortions which influence the whole cell.

Since an In or Y dopant is coordinated by 6 oxide ions, the proton-repulsive zone in the first shell affects a fraction of all O in the lattice which is approximately twice as high as the dopant concentration, i.e. for 10–20 % Y doping 20–40 % of the oxide ions are disfavoured for protonation. This is indicated by O coloured in red and violet in Fig. 9. On one hand the Y concentration should be 12 % or larger (moving towards the experimentally determined solubility limit [14]) to enable an overlap of the second-shell trapping zones (Fig. 9a). On the other hand an increasing Y content excludes more and more O from protonation (Fig. 9b; the Y arrangement in Fig. 9c excludes an entire plane from protonation). The fact that the  $\text{P3} \rightarrow \text{P3}$  barrier within the second shell (trapping zone) is higher than the barrier at large distance from Y (table S2) also decelerates long-range transport.

To model the long-range proton transport in such a complex energy landscape in more detail and more quantitatively, next-level theoretical approaches beyond static DFT are required. These could either be ab-

initio molecular dynamics (with sufficiently large cells and long time for good event statistics), or faster approaches such as Kinetic Monte Carlo simulations [25,74,75]. However, such simulations also need to be further developed beyond the approaches that were successful for example for Y-doped  $\text{BaZrO}_3$  [25]. In [25], the site energy landscape could well be approximated by a two-state model depending only on the distance to Y, and a set of 8 barriers (defined via distance to one or two Y) was sufficient to model the distribution of proton barriers. For Y-doped  $\text{BaFeO}_3$  at realistic dopant concentrations, situations need to be explored in which e.g. an O is first shell to one Y (repulsive zone) and simultaneously second shell to a neighboring Y (trapping zone), or first-shell to two Y (probably even more repulsive). Even in absence of a second dopant, the assignment to a shell around the dopant does not suffice to describe the site energy: for example configurations P1,P3 in Fig. 8b have a significantly lower energy than P4,P6 despite all belonging to the second shell. The energy is also related to the dopant being located in the  $\text{Fe-O-H} \cdots \text{O-Fe}$  plane or not, which affects the local distortions and hydrogen bonding feasibilities. Furthermore, the attempt frequencies for proton transfer, closely related to the  $\text{ODopO}$  or  $\text{OFeO}$  deformation vibrations [13,69], might vary when the proton moves around the  $\text{Dop}^{3+}$  or around Fe.

#### 4. Conclusions

In  $\text{BaFeO}_3$ , significant defect interactions between protons and B-site dopants are observed.  $\text{Ga}^{3+}$  and  $\text{Sc}^{3+}$ , which are only slightly to moderately oversized relative to Fe, show slight trapping in the first and second shell around the dopant. The larger dopants  $\text{In}^{3+}$  and  $\text{Y}^{3+}$  lead to a repulsive interaction in the first shell, demonstrating the strong impact of local geometry modifications (increased  $\text{O} \cdots \text{O}$  distances). The expansion of the  $\text{FeOHFe}$  connection upon protonation further contributes to this repulsion. This is the first example in perovskites where the interaction with a dopant leads to an exclusion sphere around the dopant instead of attraction. The various local lattice distortions caused by the dopants lead to a wide spread of proton transfer barriers. Nevertheless, the correlation to changes of O-H bond length and  $\text{O}_a \cdots \text{O}_b$  distance derived for undoped  $\text{BaFeO}_{3.5}$  remain valid (i.e. lower barriers for smaller  $\Delta\text{O-H}$  and  $\Delta\text{O} \cdots \text{O}$  values). The proton barrier in the first shell around  $\text{Ga}^{3+}$  is significantly lower than expected from these correlations, which is attributed to decreased repulsion of the proton in the transition state. The varying proton site energies and transfer barriers together lead to a very complex energy landscape. A qualitative discussion indicates that very strongly oversized dopants such as  $\text{Y}^{3+}$  with

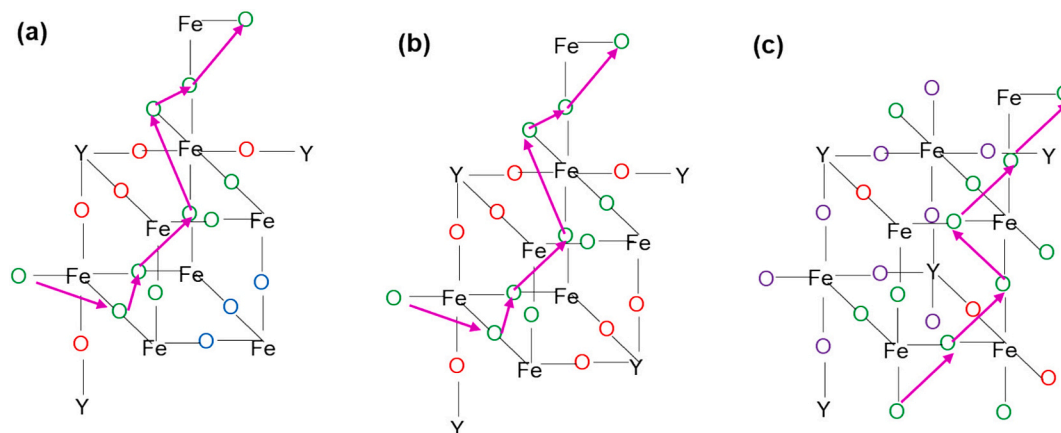


**Fig. 9.** Semiquantitative sketch of proton transfer in Y-doped  $\text{BaFeO}_3$  considering the trapping energies and the magnitude of transfer barriers for the different shells. (a) 12.5 % Y arranged to maximize Y...Y distances, (b) 25 % Y, arranged along the space diagonal, (c) 25 % Y, arranged along the face diagonal. Red O = 1. shell, green = 2. shell, blue = 3. shell around Y. Violet O in (c) are 1. shell relative to one and 2. shell relative to a neighboring Y. The relative energy for this situation is not calculated so far, but probably also high. The pink arrows correspond to P3-P3 and P4-P4 barriers within the second shell. (For interpretation of the references to colour in this figure legend, the reader is referred to the web version of this article.)

proton exclusion in the first shell and comparably large barriers in the second shell are detrimental for long-range proton transport, as this induces detours around such exclusion zones and has the potential to largely interrupt long-range proton paths. To optimize the proton conductivity of triple-conducting perovskites, a good compromise between hydration thermodynamics, distribution of proton site energies and relevant transfer barriers is required, which rather calls for only moderately oversized dopants.

### CRedit authorship contribution statement

**A. Chesnokov:** Writing – review & editing, Investigation. **D. Gryaznov:** Writing – review & editing, Writing – original draft, Supervision, Methodology, Investigation, Funding acquisition, Conceptualization. **E.A. Kotomin:** Writing – review & editing, Funding acquisition. **J. Maier:** Writing – review & editing. **R. Merkle:** Writing – review & editing, Writing – original draft, Methodology, Conceptualization.

### Declaration of competing interest

The authors declare that they have no known competing financial interests or personal relationships that could have appeared to influence the work reported in this paper.

### Acknowledgements

DFT calculations were performed at the HLRS, University of Stuttgart, within the project 12939 DEFTD. A.C. and D.G. thank the Latvian Council of Science (grant no. lzp-2021/1-0203) for financial support, and E. K. the M-Era.Net project HetCat. The Institute of Solid State Physics, University of Latvia (Latvia) as Centre of Excellence has received funding from the European Union Horizon 2020 Framework Programme H2020-WIDESPREAD-01-2016-2017-Teaming Phase2 under grant agreement No. 739508, project CAMART<sup>2</sup>.

### Appendix A. Supplementary data

Supplementary data to this article can be found online at <https://doi.org/10.1016/j.ssi.2025.116788>.

### Data availability

Data will be made available on request.

### References

- [1] C. Duan, R. Kee, H. Zhu, N. Sullivan, L. Zhu, L. Bian, D. Jennings, R. O'Hayre, Highly efficient protonic ceramic electrochemical cells for power generation and fuel production, *Nat. Energy* 230 (2019) 230–240.
- [2] M. Papac, V. Stevanovic, A. Zakutayev, R. O'Hayre, Triple ionic-electronic conducting oxides for next-generation electrochemical devices, *Nat. Mater.* 20 (2021) 301–313.
- [3] S. Choi, T.C. Davenport, S.M. Haile, Protonic ceramic electrochemical cells for hydrogen production and electricity generation: exceptional reversibility, stability, and demonstrated faradaic efficiency, *Energy Environ. Sci.* 12 (2019) 206–215.
- [4] R. Merkle, M.F. Hoedl, G. Raimondi, R. Zohourian, J. Maier, Oxides with mixed protonic and electronic conductivity, *Annu. Rev. Mater. Res.* 51 (2021) 461–493.
- [5] D. Kim, I. Jeong, S. Ahn, S. Oh, H.-N. Im, H. Bae, S.-J. Song, C.-W. Lee, W.C. Jung, K.T. Lee, On the role of bimetal-doped BaCoO<sub>3-δ</sub> perovskites as highly active oxygen electrodes of protonic ceramic electrochemical cells, *Adv. Energy Mater.* 14 (2024) 2304059.
- [6] F. He, Y. Zhou, T. Hu, Y. Xu, M. Hou, F. Zhu, D. Liu, H. Zhang, K. Xu, M. Liu, Y. Chen, An efficient high-entropy perovskite-type air electrode for reversible oxygen reduction and water splitting in protonic ceramic cells, *Adv. Mater.* 35 (2023) 2209469.
- [7] Y. Wang, Y. Ling, B. Wang, G. Zhai, G. Yang, Z. Shao, R. Xiao, T. Li, A review of progress in proton ceramic electrochemical cells: material and structural design, coupled with value-added chemical production, *Energy Environ. Sci.* 16 (2023) 5721–5770.
- [8] R. Strandbakke, V.A. Cherepanov, A.Y. Zuev, D.S. Tsvetkov, C. Argiris, G. Sourkouni, S. Prünke, T. Norby, Gd- and Pr-based double perovskite cobaltites as oxygen electrodes for proton ceramic fuel cells and electrolyser cells, *Solid State Ionics* 278 (2015) 120–132.
- [9] Z. Wang, W. Yang, S.P. Shafi, L. Bi, Z. Wang, R. Peng, C. Xia, W. Liu, Y. Lu, A high performance cathode for proton conducting solid oxide fuel cells, *J. Mater. Chem. A* 3 (2015) 8405–8412.
- [10] A.P. Tarutin, J.G. Lyagaeva, D.A. Medvedev, L. Bi, A.A. Yaremchenko, Recent advances in layered Ln<sub>2</sub>NiO<sub>4+δ</sub> nickelates: fundamentals and prospects of their applications in protonic ceramic fuel and electrolysis cells, *J. Mater. Chem. A* 9 (2021) 154–195.
- [11] J.A. Kilner, R.J. Brook, A study of oxygen ion conductivity in doped nonstoichiometric oxides, *Solid State Ionics* 6 (1982) 237–252.
- [12] R.A. De Souza, Oxygen diffusion in SrTiO<sub>3</sub> and related perovskite oxides, *Adv. Funct. Mater.* 25 (2015) 6326–6342.
- [13] K.D. Kreuer, Proton-conducting oxides, *Annu. Rev. Mater. Sci.* 33 (2003) 333–359.
- [14] R. Zohourian, R. Merkle, G. Raimondi, J. Maier, Mixed-conducting perovskites as cathode materials for protonic ceramic fuel cells: understanding the trends in proton uptake, *Adv. Funct. Mater.* 28 (2018) 1801241.
- [15] G. Raimondi, R. Merkle, J. Maier, Impact of first-row transition metals in (Ba,La)(Fe,TM)O<sub>3-δ</sub> on proton uptake and electronic conductivity, *Solid State Ionics* 391 (2023) 116143.
- [16] M.F. Hoedl, A. Chesnokov, D. Gryaznov, R. Merkle, E.A. Kotomin, J. Maier, Proton migration barriers in BaFeO<sub>3-δ</sub> - insights from DFT calculations, *J. Mater. Chem. A* 11 (2023) 6336–6348.
- [17] K.D. Kreuer, S. Adams, W. Münch, A. Fuchs, U. Klock, J. Maier, Proton conducting alkaline earth zirconates and titanates for high drain electrochemical applications, *Solid State Ionics* 145 (2001) 295–306.
- [18] M. Shirpour, R. Merkle, J. Maier, Space charge depletion in grain boundaries of BaZrO<sub>3</sub> proton conductors, *Solid State Ionics* 225 (2012) 304–307.
- [19] Y. Yamazaki, F. Blanc, Y. Okuyama, L. Buannic, J.C. Lucio-Vega, C.P. Grey, S. M. Haile, Proton trapping in yttrium-doped barium zirconate, *Nat. Mater.* 12 (2013) 647–651.
- [20] F. Blanc, L. Sperrin, D. Lee, R. Dervişoğlu, Y. Yamazaki, S.M. Haile, G. De Paëpe, C. P. Grey, Dynamic nuclear polarization NMR of low-γ nuclei: structural insights into hydrated yttrium-doped BaZrO<sub>3</sub>, *J. Phys. Chem. Lett.* 5 (2014) 2431–2436.
- [21] L. Buannic, L. Sperrin, R. Dervişoğlu, F. Blanc, C.P. Grey, Proton distribution in Sc-doped BaZrO<sub>3</sub>: a solid state NMR and first principle calculations analysis, *Phys. Chem. Chem. Phys.* 20 (2018) 4317–4328.
- [22] M.E. Bjorketun, P.G. Sundell, G. Wahnstrom, Effect of acceptor dopants on the proton mobility in BaZrO<sub>3</sub>: a density functional investigation, *Phys. Rev. B* 76 (2007) 054307.
- [23] H. Takahashi, I. Yashima, K. Amezawa, K. Eguchi, H. Matsumoto, H. Takamura, S. Yamaguchi, First-principles calculations for the energetics of the hydration reaction of acceptor-doped BaZrO<sub>3</sub>, *Chem. Mater.* 29 (2017) 1518–1526.
- [24] Y. Yamazaki, A. Kuwabara, J. Hyodo, Y. Okuyama, C.A.J. Fisher, S.M. Haile, Oxygen affinity: the missing link enabling prediction of proton conductivities in doped barium Zirconates, *Chem. Mater.* 32 (2020) 7292–7300.
- [25] F.M. Draber, C. Ader, J.P. Arnold, S. Eisele, S. Grieshammer, S. Yamaguchi, M. Martin, Nanoscale percolation in doped BaZrO<sub>3</sub> for high proton mobility, *Nat. Mater.* 19 (2020) 338–346.
- [26] G. Raimondi, F. Giannici, A. Longo, R. Merkle, A. Chiara, M.F. Hoedl, A. Martorana, J. Maier, X-ray spectroscopy of (Ba,Sr,La)(Fe,Zn,Y)O<sub>3-δ</sub> identifies structural and electronic features favoring proton uptake, *Chem. Mater.* 32 (2020) 8502–8511.
- [27] G. Raimondi, A. Longo, F. Giannici, R. Merkle, M.F. Hoedl, A. Chiara, C.J. Sahle, J. Maier, Electronic modifications in (Ba,La)(Fe,Zn,Y)O<sub>3-δ</sub> unveiled by Oxygen K-edge X-Ray Raman Scattering, *J. Mater. Chem. A* 10 (2022) 8866–8876.
- [28] Z. Wang, W. Yang, Z. Zhu, R.R. Peng, X. Wu, C. Xi, Y. Lu, First-principles study of O<sub>2</sub> reduction on BaZr<sub>1-x</sub>Co<sub>x</sub>O<sub>3</sub> cathodes in protonic-solid oxide fuel cells, *J. Mater. Chem. A* 2 (2014) 16707–16714.
- [29] A.B. Munoz-Garcia, M. Pavone, First-principles design of new electrodes for proton-conducting solid-oxide electrochemical cells: A-site doped Sr<sub>2</sub>Fe<sub>1.5</sub>Mo<sub>0.5</sub>O<sub>6-δ</sub> perovskite, *Chem. Mater.* 28 (2016) 490–500.
- [30] H. Ding, W. Wu, C. Jiang, Y. Ding, W. Bian, B. Hu, P. Singh, C.J. Orme, L. Wang, Y. Zhang, D. Ding, Self-sustainable protonic ceramic electrochemical cells using a triple conducting electrode for hydrogen and power production, *Nat. Commun.* 11 (2020) 1907.
- [31] Z. Wang, Y. Wang, J. Wang, Y. Song, M.J. Robson, A. Seong, M. Yang, Z. Zhang, A. Belotti, J. Liu, G. Kim, J. Lim, Z. Shao, F. Ciucci, Rational design of perovskite ferrites as high-performance proton-conducting fuel cell cathodes, *Nat. Cat.* 5 (2022) 777–787.
- [32] R. Jinnouchi, K. Miwa, F. Karsai, G. Kresse, R. Asahi, On-the-fly active learning of interatomic potentials for large-scale atomistic simulations, *J. Phys. Chem. Lett.* 11 (2020) 6946–6955.
- [33] L.C. Erhard, J. Rohrer, K. Albe, V.L. Deringer, A machine-learned interatomic potential for silica and its relation to empirical models, *npj Comput. Mater.* 8 (2022) 90.
- [34] Y. Yang, S. Zhang, K.D. Ranasinghe, O. Isayev, A.E. Roitberg, Machine learning of reactive potentials, *Annu. Rev. Phys. Chem.* 75 (2024) 371–395.
- [35] C. Zhang, L. Tang, Y. Sun, K.-M. Ho, R.M. Wentzcovitch, C.-Z. Wang, Deep machine learning potential for atomistic simulation of Fe-Si-O systems under Earth's outer core conditions, *Phys. Rev. Mater.* 6 (2022) 063802.
- [36] Z. Li, Z. Hu, Y. Wang, R. Ouyang, Molecular dynamics simulation of Co-Fe-based perovskite oxide/water interfaces, *J. Phys. Chem. C* 128 (2024) 10035–10041.
- [37] R.D. Shannon, Revised effective ionic radii and systematic studies of interatomic distances in halides and chalcogenides, *Acta Crystallogr. A* 32 (1976) 751–767.
- [38] D.W. Smith, An acidity scale for binary oxides, *J. Chem. Educ.* 64 (1987) 480–481.

- [39] R. Merkle, M.F. Hoedl, A. Chesnokov, D. Gryaznov, E. Bucher, E.A. Kotomin, W. Sitte, J. Maier, Electronic structure, phase formation, and defect distribution in the Ba(Ce,Fe,Acc)O<sub>3-δ</sub> system, 2024 submitted.
- [40] G. Kresse, J. Hafner, Ab-initio molecular dynamics for liquid metals, *Phys. Rev. B* 47 (1993) 558–561.
- [41] G. Kresse, J. Furthmüller, Efficiency of ab-initio total energy calculations for metals and semiconductors using a plane-wave basis set, *Comput. Mater. Sci.* 6 (1996) 15–50.
- [42] G. Kresse, J. Furthmüller, Efficient iterative schemes for ab-initio total-energy calculations using a plane-wave basis set, *Phys. Rev. B* 54 (1996) 11169–11186.
- [43] P.E. Blöchl, Projector augmented-wave method, *Phys. Rev. B* 50 (1994) 17953–17979.
- [44] M.F. Hoedl, D. Gryaznov, R. Merkle, E.A. Kotomin, J. Maier, Interdependence of oxygenation and hydration of mixed conducting (Ba,Sr)FeO<sub>3-δ</sub> perovskites studied by density functional theory, *J. Phys. Chem. C* 124 (2020) 11780–11789.
- [45] J.P. Perdew, K. Burke, M. Ernzerhof, Generalized gradient approximation made simple, *Phys. Rev. Lett.* 77 (1996) 3865–3868.
- [46] S. Dudarev, G. Botton, S. Savrasov, C. Humphreys, A. Sutton, Electron-energy-loss spectra and the structural stability of nickel oxide: an LSDA+U study, *Phys. Rev. B* 57 (1998) 1505–1509.
- [47] B. Ribeiro, M. Godinho, C. Cardoso, R. Borges, T. Gasche, Self-doping and the role of oxygen vacancies in the magnetic properties of cubic BaFeO<sub>3-δ</sub>, *J. Appl. Phys.* 113 (2013) 083906.
- [48] Y. Lee, J. Kleis, J. Rossmeisl, D. Morgan, Ab initio energetics of LaBO<sub>3</sub> (001) (B=Mn, Fe, Co, and Ni) for solid oxide fuel cell cathodes, *Phys. Rev. B* 80 (2009) 224101.
- [49] Z. Baiyee, C. Chen, F. Ciucci, A DFT+U study of A-site and B-site substitution in BaFeO<sub>3-δ</sub>, *Phys. Chem. Chem. Phys.* 17 (2015) 23511–23520.
- [50] Y.-L. Lee, J. Kleis, J. Rossmeisl, D. Morgan, *Ab initio* energetics of LaBO<sub>3</sub>(001) (B=Mn, Fe, Co, and Ni) for solid oxide fuel cell cathodes, *Phys. Rev. B* 80 (2009) 224101.
- [51] A.J. Jacobson, Powder neutron-diffraction study of structure and oxygen vacancy distribution in 6H BaFeO<sub>2.79</sub>, *Acta Cryst B* 32 (1976) 1087–1090.
- [52] N. Hayashi, T. Yamamoto, H. Kageyama, M. Nishi, Y. Watanabe, T. Kawakami, Y. Matsushita, A. Fujimori, M. Takano, BaFeO<sub>3</sub>: a ferromagnetic iron oxide, *Angew. Chem.* 123 (2011) 12755–12758.
- [53] C. Chen, D. Chen, Y. Gao, Z. Shao, F. Ciucci, Computational and experimental analysis of Ba<sub>0.95</sub>La<sub>0.05</sub>FeO<sub>3-δ</sub> as a cathode material for solid oxide fuel cells, *J. Mater. Chem. A* 2 (2014) 14154–14163.
- [54] M. Abbate, H. Ascolani, F. Prado, A. Caneiro, Electronic structure and band gap of the negative charge-transfer material Sr<sub>3</sub>Fe<sub>2</sub>O<sub>7</sub>, *Sol. St. Comm.* 129 (2004) 113–116.
- [55] A. Cammarata, J.M. Rondinelli, Octahedral engineering of orbital polarizations in charge transfer oxides, *Phys. Rev. B* 87 (2013) 155135.
- [56] H. Jónsson, G. Mills, K.W. Jacobsen, Nudged elastic band method for finding minimum energy paths of transitions, in: B.J. Berne, G. Ciccotti, D.F. Coker (Eds.), *Classical and Quantum Dynamics in Condensed Phase Simulations*, World Scientific, Singapore, 1998.
- [57] G. Henkelman, B.P. Uberuaga, H. Jónsson, A climbing image nudged elastic band method for finding saddle points and minimum energy paths, *J. Chem. Phys.* 113 (2000) 9901–9904.
- [58] A. Van der Ven, G. Ceder, M. Asta, P.D. Tepeesch, First-principles theory of ionic diffusion with nondilute carriers, *Phys. Rev. B* 64 (2001) 184307.
- [59] A. Torayev, L. Sperrin, M.A. Gomez, J.A. Kattirtzi, C. Merlet, C.P. Grey, Local distortions and dynamics in hydrated Y-doped BaZrO<sub>3</sub>, *J. Phys. Chem. C* 124 (2020) 16689–16701.
- [60] T.S. Bjorheim, M.F. Hoedl, R. Merkle, E.A. Kotomin, J. Maier, Proton, hydroxide ion, and oxide ion affinities of closed-shell metal oxides: importance for the hydration reaction and correlation to electronic structure, *J. Phys. Chem. C* 124 (2020) 1277–1284.
- [61] I. Olovsson, P.-G. Jönsson, in: P. Schuster, G. Zundel, C. Sandorfy (Eds.), *The Hydrogen Bond: Recent Developments in Theory and Experiments*, North-Holland, 1976 chapter 8.
- [62] H. Alig, J. Lösel, M. Trömel, Zur Kristallchemie der Wasserstoff-Sauerstoff-Bindungen, *Z. Krist.* 209 (1994) 18–21.
- [63] T. Steiner, W. Saenger, Lengthening of the covalent O-H bond in O-H<sup>+</sup> hydrogen bonds re-examined from low-temperature neutron diffraction data of organic compounds, *Acta Crystallogr. B* 50 (1994) 348–357.
- [64] G.C. Pimentel, A.L. McClellan, Hydrogen bonding, *Annu. Rev. Phys. Chem.* 22 (1971) 347–385.
- [65] R. Merkle et al. (2024) in preparation.
- [66] W. Munch, K.-D. Kreuer, G. Seifert, J. Maier, A quantum molecular dynamics study of proton diffusion in SrTiO<sub>3</sub> and CaTiO<sub>3</sub>, *Solid State Ionics* 125 (1999) 39–45.
- [67] M.A. Gomez, M.A. Griffin, S. Jindal, K.D. Rule, V.R. Cooper, The effect of octahedral tilting on proton binding sites and transition states in pseudo-cubic perovskite oxides, *J. Chem. Phys.* 123 (2005) 094703.
- [68] P.G. Sundell, M.E. Bjorketun, G. Wahnstrom, Density-functional calculations of prefactors and activation energies for H diffusion in BaZrO<sub>3</sub>, *Phys. Rev. B* 76 (2007) 094301.
- [69] M. F. Hoedl et al., in preparation (2024).
- [70] G. Winterhoff, S. Neitzel-Grieshammer, A review of proton migration and interaction energies in doped barium zirconate, *Solid State Ionics* 397 (2023) 116231.
- [71] J. Hyodo, K. Kitabayashi, K. Hoshino, Y. Okuyama, Y. Yamazaki, Fast and stable proton conduction in heavily scandium-doped polycrystalline barium Zirconate at intermediate temperatures, *Adv. Energy Mater.* 10 (2020) 2000213.
- [72] F. Draber, PhD thesis. RWTH Aachen, Germany, 2021, <https://doi.org/10.18154/RWTH-2021-03399>, <https://publications.rwth-aachen.de/record/816722>.
- [73] F.M. Draber, J.R. Denninger, P.C. Müller, I.K. Sommerfeld, M. Martin, The impact of nanoscale percolation in yttrium-doped BaZrO<sub>3</sub> on the oxygen ion and proton conductivities: a density functional theory and kinetic Monte Carlo Study, *Adv. Energ. Sust. Res.* 3 (2022) 2200007.
- [74] A.D. Murray, G.E. Murch, C.R.A. Catlow, A new hybrid scheme of computer simulation based on HADES and Monte Carlo: application to ionic conductivity in Y<sup>3+</sup> doped CeO<sub>2</sub>, *Solid State Ionics* 18 (1986) 196–202.
- [75] S. Grieshammer, B.O.H. Grope, J. Koettgen, M. Martin, A combined DFT + U and Monte Carlo study on rare earth doped ceria, *Phys. Chem. Chem. Phys.* 16 (2014) 9974.